



HAL
open science

Two-step cycling process alternating implantation and remote plasma etching for topographically selective etching: Application to Si₃N₄ spacer etching

Vincent Renaud, Camille Petit-Etienne, Jean-Paul Barnes, Jérémie Bissierier, Olivier Joubert, Erwine Pargon

► To cite this version:

Vincent Renaud, Camille Petit-Etienne, Jean-Paul Barnes, Jérémie Bissierier, Olivier Joubert, et al.. Two-step cycling process alternating implantation and remote plasma etching for topographically selective etching: Application to Si₃N₄ spacer etching. *Journal of Applied Physics*, 2019, 126 (24), pp.243301. 10.1063/1.5131030 . halshs-02428534

HAL Id: halshs-02428534

<https://shs.hal.science/halshs-02428534>

Submitted on 6 Nov 2020

HAL is a multi-disciplinary open access archive for the deposit and dissemination of scientific research documents, whether they are published or not. The documents may come from teaching and research institutions in France or abroad, or from public or private research centers.

L'archive ouverte pluridisciplinaire **HAL**, est destinée au dépôt et à la diffusion de documents scientifiques de niveau recherche, publiés ou non, émanant des établissements d'enseignement et de recherche français ou étrangers, des laboratoires publics ou privés.

Two-step cycling process alternating implantation and remote plasma etching for topographically selective etching: Application to Si_3N_4 spacer etching

Cite as: J. Appl. Phys. **126**, 243301 (2019); <https://doi.org/10.1063/1.5131030>

Submitted: 08 October 2019 . Accepted: 05 December 2019 . Published Online: 23 December 2019

Vincent Renaud,  Camille Petit-Etienne, Jean-Paul Barnes, Jérémie Bisselier, Olivier Joubert, and Erwine Pargon



View Online



Export Citation



CrossMark

ARTICLES YOU MAY BE INTERESTED IN

[Thin layer etching of silicon nitride: A comprehensive study of selective removal using \$\text{NH}_3/\text{NF}_3\$ remote plasma](#)

Journal of Vacuum Science & Technology A **34**, 061301 (2016); <https://doi.org/10.1116/1.4963072>

[Overview of atomic layer etching in the semiconductor industry](#)

Journal of Vacuum Science & Technology A **33**, 020802 (2015); <https://doi.org/10.1116/1.4913379>

[Fluorocarbon based atomic layer etching of \$\text{Si}_3\text{N}_4\$ and etching selectivity of \$\text{SiO}_2\$ over \$\text{Si}_3\text{N}_4\$](#)

Journal of Vacuum Science & Technology A **34**, 041307 (2016); <https://doi.org/10.1116/1.4954961>

Meet the Next Generation
of Quantum Analyzers

And Join the Launch
Event on November 17th



Register now



Zurich
Instruments

Two-step cycling process alternating implantation and remote plasma etching for topographically selective etching: Application to Si₃N₄ spacer etching

Cite as: J. Appl. Phys. **126**, 243301 (2019); doi: [10.1063/1.5131030](https://doi.org/10.1063/1.5131030)

Submitted: 8 October 2019 · Accepted: 5 December 2019 ·

Published Online: 23 December 2019




View Online



Export Citation



CrossMark

Vincent Renaud,¹ Camille Petit-Etienne,¹  Jean-Paul Barnes,² Jérémie Bissierier,³ Olivier Joubert,¹ and Erwine Pargon^{1,a)}

AFFILIATIONS

¹Univ. Grenoble Alpes, CNRS, CEA/LETI Minatec, LTM, 38000 Grenoble, France

²Univ. Grenoble Alpes, CEA/LETI Minatec, 38000 Grenoble, France

³Applied Materials France, 864 chemin des Fontaines, 38190 Bernin, France

^{a)}Electronic mail: erwine.pargon@cea.fr

ABSTRACT

This article proposes an original method to achieve topographically selective etching. It relies on cycling a two-step process comprising a plasma implantation step and a removal etching step using remote plasma source process. Both steps can be achieved in the same reactor prototype chamber, which has the capability to produce both capacitively coupled plasma and remote plasma (RP) discharges. It is shown that in RP processes, an incubation time exists before the etching starts. The introduction of a plasma implantation step prior to the RP step allows us to selectively functionalize the horizontal surfaces of the material with respect to the vertical surfaces, thanks to the ion directionality. The modifications induced by the implantation allow us to modify the incubation time between an implanted and a nonimplanted material offering a process window with infinite etch selectivity between horizontal and vertical surfaces. This approach has been demonstrated on Si₃N₄ blanket films with the perspective to be applied to the Si₃N₄ spacer etching process in which etch selectivity is a key issue. For this particular application, a cycling process comprising an H₂ plasma implantation and a He/NH₃/NF₃ remote plasma process has been developed. The H₂ implantation modifies the Si₃N₄ surface state by incorporating oxygen contaminants coming from the reactor wall and creating dangling bonds. This surface functionalization considerably reduces the incubation time. New insights into the etching mechanisms of Si₃N₄ films exposed to NH₃/NF₃ remote plasma are proposed and explain why the presence of Si–O bonds is mandatory for the initiation of the etching.

Published under license by AIP Publishing. <https://doi.org/10.1063/1.5131030>

I. INTRODUCTION

The increasing complexity in fabricating devices consisting of various layers of nanoscale materials, and 3D features have led to the need for processing materials in a selective manner.¹ Past few years, both academia and industry are looking for new process technologies allowing us to make atomic scale processing techniques, such as atomic layer deposition (ALD) and atomic layer etching (ALE), more selective.^{2,3} Similar to the growing field of selective area deposition,^{4,5} etch selectivity could be classified into two categories: area selective chemical etching and topographically

selective etching. In the first case, the etch selectivity arises from a difference in the chemical affinity of the reactive neutrals with the present materials and with no preferential etching direction. In the second case, it refers to the ability to etch a material selectively with respect to itself in a preferential direction, i.e., etch the horizontal surfaces of a material selectively over vertical surfaces or vice versa.

In particular, the silicon nitride spacer etching process, which is considered one of the most challenging steps of Metal-Oxide-Semiconductor (MOS) transistor fabrication technologies, requires

these two kinds of selectivities. On the one hand, the spacer process must enable the Si_3N_4 spacer removal on horizontal surfaces (top and bottom of the pattern) without consuming the spacer sidewalls (vertical surfaces), and this is a very anisotropic way to generate straight spacer profiles. On the other hand, it must provide an extremely high chemical etch selectivity over the underneath silicon or silicon germanium in order to minimize the consumption of these materials in the source/drain regions. Minimizing the silicon recess and ion-induced damages to silicon surfaces are key criteria to ensure a high surface quality for the subsequent step of silicon or SiGe epitaxy.

Conventional plasma etching techniques based on CHF_3/O_2 continuous wave (CW) plasma^{6,7} showed some intrinsic limitations to remove silicon nitride on horizontal surfaces without inducing either critical dimension loss or Si/SiGe source/drain recess.⁸ Indeed, the ion-neutral synergy that drives the etching mechanism in CW plasma induces the creation of a few-nanometer-thick reactive layers (ion energies >15 – 20 eV), which compromise the etch precision.⁹ Blanc *et al.* showed that improved spacer process performance can be obtained by using synchronous pulsed plasma technology.¹⁰ The switching on and off in a synchronous manner of both the source and bias powers at a low duty cycle allows us to decrease the average ion energy and the plasma chemical reactivity (more molecular than atomic), which ultimately reduce plasma induced damage. Although they showed that pulsed plasma process leads to minimized silicon recess and improved spacer profiles compared to CW plasma processes, the spacer process performance is still not satisfactory for advanced technology nodes.^{11,12}

More recently, Posseme *et al.* proposed an interesting approach for the etching of a silicon nitride spacer with anisotropic sidewalls and minimal induced damage.¹³ This process, called “smart etch” hereafter, consists of two sequential steps.¹⁴ In the first step, the Si_3N_4 film is anisotropically modified by a light ion implantation (typically H_2 or He) achieved either in an inductively coupled plasma (ICP) or capacitive coupled plasma (CCP) reactor. The layer modification depth is driven by the ion energy, while its chemical composition is determined by the ion dose.¹⁴ In a second step, the modified layer can be selectively removed by using an HF reactant either in a liquid solution¹⁴ or in gas phase (followed by water rinsing)^{15,16} or by using $\text{NH}_3/\text{NF}_3/\text{He}$ remote plasmas (RPs) followed by an annealing step.¹⁷ For all these removal techniques, the etching of the modified Si_3N_4 layer proceeds with the formation of ammonium hexafluorosilicate salts $[(\text{NH}_4)_2\text{SiF}_6]$ ^{15–18} that are subsequently either dissolved in water (when HF is used) or outgassed by annealing (when NH_3/NF_3 remote plasma is used). Posseme *et al.* showed that removal with liquid HF and with NH_3/NF_3 remote plasma has one major weakness in that it does not provide any selectivity to silicon dioxide.^{14,17} On the contrary, gaseous HF removal can provide a high selectivity between modified Si_3N_4 and SiO_2 but faces some queue time issues between the gaseous HF exposure and the aqueous phase removal.^{15,16} A too long queue time between those two steps leads to some residues that are difficult to remove. Moreover, in all the approaches proposed by Posseme *et al.*, the two-step process requires at least the use of two different and separated equipment, implying an air exposure between the two steps. Another drawback is that the

implantation step must be well calibrated to modify in one shot the targeted thickness to be etched. Cycles of the two steps could be envisaged to solve this issue, but it will require back and forth between the implantation reactor and the equipment used to remove the modified layer, compromising the process throughput. Sherpa *et al.*^{19,20} proposed to cycle the two steps in the same capacitive plasma reactor. H_2 plasma at 20 mTorr was used for the implantation step, while fluorinated plasma such as NF_3 or SF_6 at high pressure (>500 mTorr) was proposed for the selective removal step. By operating the second step at high pressure, they expected to lower ion to neutral flux ratio and to minimize the ionic bombardment in order to favor a chemical and selective type of etching. In their case, the etching of the silicon nitride films during the second step does not proceed with the formation of a salt layer but is mainly driven by the chemical reactivity of atomic fluorine with SiN, SiH, or NH bonds based on thermodynamical considerations. Using this approach, they showed that the etch rate of the H_2 implanted silicon nitride increases almost tenfold compared to the etch rate of pristine silicon nitride in the fluorinated plasma. They also mentioned that the etch selectivity to silicon oxide is superior to 100, confirming the negligible role of ionized species in the fluorinated capacitive discharge at 500 mTorr. However, although not discussed in their article, we suspect that the process will not be selective over silicon if indeed the mechanisms are driven by atomic fluorine.

In this article, we propose a new route to implement the smart etch concept by cycling the two steps of the process in the same plasma reactor chamber that has the capability to produce both a CCP discharge for the implantation step and a remote plasma discharge in which only neutral species are involved for the removal step.

In Sec. II of this article, the experimental setup and characterization techniques will be described. The experimental results will be presented and discussed in Sec. III as follows. First, in Sec. III A, the modifications induced in a Si_3N_4 film by H_2 or He implantation will be revisited and compared to previously published experimental and simulated works. One key result is that the oxygen coming from chamber contamination is incorporated into Si_3N_4 and that this involuntary contamination plays a key role in the subsequent step. Secondly, in Sec. III B, the etching kinetics of implanted and nonimplanted Si_3N_4 films exposed to He/ NH_3/NF_3 remote plasma (RP) will be studied by *in situ* kinetic ellipsometry. In this section, we will propose new insights into the etching mechanisms of Si_3N_4 films exposed to NH_3/NF_3 remote plasma. We will show that RP processes are strongly sensitive to the material surface state and that an incubation time exists before the etching starts. We will especially highlight the key role of the presence of oxygen on the Si_3N_4 surface on the catalysis of the reaction. The introduction of an implantation allows us to functionalize the material surface and thus activate the species adsorption and reaction reducing the incubation time considerably. This offers a process window where the selectivity between implanted and non-implanted SiN is infinite. Finally, in Sec. III C, we will demonstrate how the cycling of the two steps, implantation followed by RP etching, can be implemented to achieve topographically selective etching, which is one key criteria of the spacer etching process development.

II. EXPERIMENTAL

A. Substrates

The Si_3N_4 films used in this study are 55 nm-thick and are deposited by low-pressure chemical vapor deposition (LPCVD) at 780 °C on a 10.5 nm-thick LPCVD silicon oxide itself deposited at 200 °C on a 300 mm diameter Si wafer. A silicon on insulator wafer with a 80 nm-thick Si layer (buried oxide layer thickness of 145 nm) is also used to investigate the etch kinetics of Si materials exposed to NH_3/NF_3 remote plasma in Sec. III C.

B. Plasma reactor

The experiments are carried out in a 300 mm prototype etch chamber from Applied Materials (cf. Fig. 1). This chamber is a hybrid plasma processing system incorporating both a remote plasma source (RPS) unit and a capacitively coupled plasma (CCP) unit. The CCP unit (lower chamber) comprises a radio frequency (RF) power supply (13.56 MHz) coupled to the bottom electrode that is equipped with an electrostatic chuck on which the substrate lies. The chuck temperature can be varied from 40 °C up to 250 °C. The RPS unit (upper chamber) consists of a RF power supply

(13.56 MHz) coupled to the top electrode and is separated from the CCP unit by a lid consisting of several showerheads. The showerheads positioned inside the chamber between the CCP and RPS units act as both a distribution component for gases and an ion suppressor that blocks the ionized species traveling through the showerhead from the plasma region to the substrate. Moreover, the lid temperature is controlled at 130 °C, and the chamber wall is held at 80 °C by a heat exchanger. The reactor chamber wall is coated with a protective layer of yttrium oxide.

In this study, the CCP unit is used to generate He or H_2 plasmas to implant ions and to induce modifications of the Si_3N_4 films. The plasma conditions used for He and H_2 implantations are given in Table I. Two plasma parameters are critical for the implantation: the ion energy that drives the ion depth penetration and thus the modified layer thickness, and the ion dose (ion flux \times time) that drives the modification rate.¹⁴ Previous studies done by molecular dynamics simulations have shown that there is an ion dose threshold to reach the steady-state modification.²¹ In this study, we have selected implantation conditions allowing to be in the steady-state regime for both He and H_2 implantations (cf. Table I). Moreover, with the implantation conditions used, the direct current voltage V_{dc} is almost similar for He and H_2 implantation, of 120 eV and 130 eV, respectively.

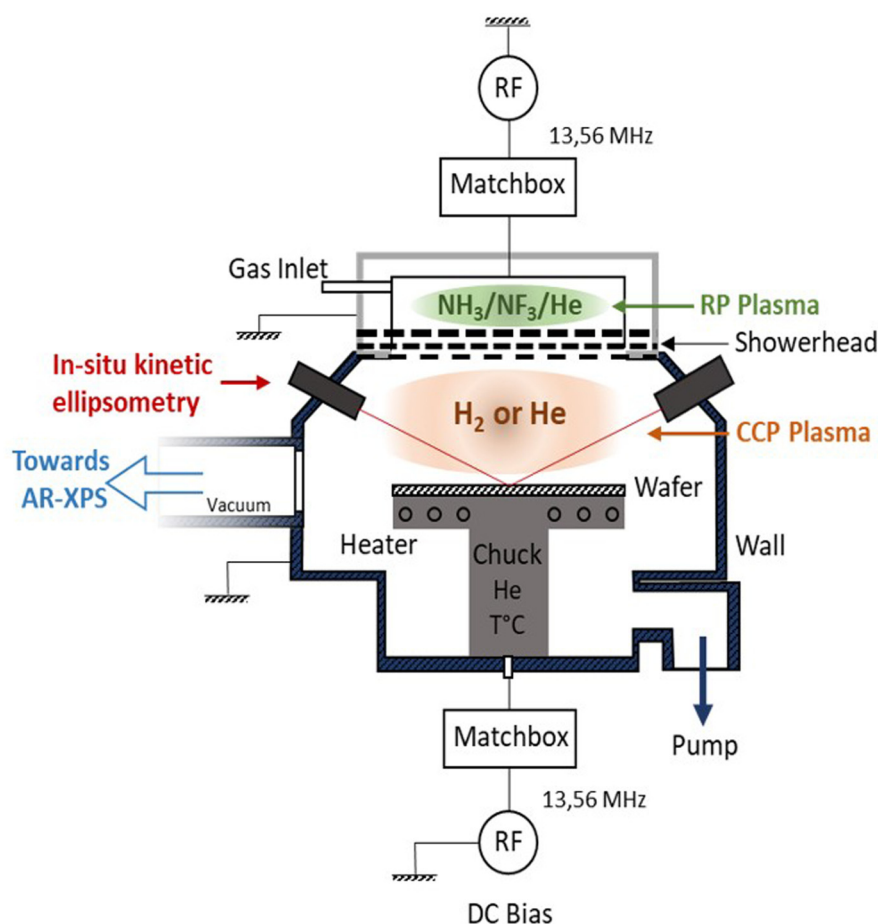


FIG. 1. Scheme of the plasma reactor prototype.

TABLE I. Plasma conditions used for the He and H₂ implantations on silicon nitride film.

	RF power (W)	Pressure (mTorr)	Process time (s)	Gas flow (sccm)	V _{dc} (V)
H ₂	50	50	60	500	130
He	50	50	60	1000	120

The RPS unit is used to perform the chemical and selective removal of the modified Si₃N₄ layers using the following plasma conditions in all the studies: NH₃: 400 sccm, NF₃: 40 sccm, He: 1400 sccm, source power: 250 W, chamber pressure: 2.5 Torr, and Chuck temperature: 60/100/120 °C.

C. Characterization techniques

X-ray reflectometry (XRR), X-ray photoelectron spectroscopy (XPS), and time-of-flight secondary ion mass spectroscopy (ToF-SIMS) were used to characterize the Si₃N₄ films after He and H₂ implantation and provide chemical and physical information on the modified Si₃N₄ layer, while kinetic ellipsometry was used to monitor the etch kinetics of implanted and nonimplanted Si₃N₄ films exposed to RP process.

1. X-ray reflectometry

X-ray reflectometry was used to measure the thickness of the Si₃N₄ modified layer after implantation. The XRR equipment (JVX5200T from Jordan Valley) uses a copper source, with a Cu-K α emission at 0.154 nm. The convergent beam angle is varied between 0° and 3.3° during the experiment. Beside the thickness, this nondestructive method of characterization allows to measure the density and the roughness of the Si₃N₄ films.

2. Angle-resolved X-ray photoelectron spectroscopy

The chemical atomic composition of the Si₃N₄ surface (about the first 10 nm) before and after implantation is characterized by quasi *in situ* angle-resolved X-ray photoelectron spectroscopy (ARXPS). A Thermo Electron Theta 300 ARXPS is directly interfaced to the etch platform via a vacuum transfer chamber. The ARXPS system is equipped with a high-resolution monochromatic Al K α x-ray source (1486.6 eV photons). The angle-resolved capability of the Theta 300 is used for all analyses, with eight angles regularly spaced between 23.75° and 76.25°, referred to the normal of the wafer. A genetic algorithm based on the maximum entropy method (provided by Thermo Fisher Scientific) is used to reconstruct atomic composition depth profiles from angle-resolved XPS data. The fitting procedure assumed that photoelectrons coming from the underlying bulk silicon are detected at a minimum emission angle of 23.75°. This allows maximizing the profile information content. Since the overlayer density is unknown after plasma treatment, the depth scale should be interpreted in a qualitative

way (i.e., relative comparison from one experiment to the other and no absolute interpretation of the depth range).²²

3. Time-of-flight secondary ion mass spectroscopy

ToF-SIMS experiments using a ToF-SIMS V instrument from ION-TOF GmbH are used to evaluate the chemical composition of the Si₃N₄ films before and after implantation over tens of nanometers in depth. With this technique, the thickness of the Si₃N₄ modified layer after implantation and the in-depth element concentration can be estimated. For the experiments, negative secondary ions are detected using a dual beam acquisition. A Bi₃ beam with an incident energy of 50 keV (0.5 nA) and a 90 × 90 μm^2 raster is used for the analysis. This beam is alternated with a positive cesium sputter beam with an energy of 500 eV (for a corresponding current of 40 nA) that was rastered over a 500 × 500 μm^2 area. We used a cycle time of 140 μs with a corresponding cycle of acquisition of 4 frames and 1 s sputtering with 1 s pause time between two acquisitions.

4. Kinetic ellipsometry

Kinetic ellipsometry is used to monitor in real time the etched thickness of the materials exposed to the RPS process. A multi-wavelength ellipsometer Uvisel from Horiba/Jobin Yvon is directly connected to the prototype reactor allowing *in situ* measurement of the material thickness. This phase-modulated ellipsometer enables *in situ* spectroscopic ellipsometry between 1.5 and 6.2 eV and real-time kinetic measurements using 32 wavelengths with a time resolution of 500 ms. The light source consists of a 75 W Xe lamp, and the light beam incident angle is of 62° to the normal of the wafer surface. The polarizer and analyzer are glan type devices with an extinction coefficient of 10⁻⁵ and an angular precision of 0.01° at a fixed angle. The thickness of the materials was calculated using the DeltaPsi II software, developed by Horiba/Jobin Yvon. It has already been reported that the etching of Si₃N₄ or SiO₂ films exposed to NH₃/NF₃ remote plasma proceeds with the formation of an ammonium hexafluorosilicate (NH₄)₂SiF₆ salt layer on their surface.^{17,23-25} Figures 2(a) and 2(b) show the scanning electronic microscopy (SEM) and atomic force microscopy (AFM) images of the salt layer formed on a Si₃N₄ film exposed to the NH₃/NF₃ RP process at 60 °C. It looks like a tangle of polycrystals separated with cracks and voids. Based on these observations, an ellipsometric model is developed to fit the bilayer composed of the unmodified Si₃N₄ film above which a salt layer is formed [cf. Fig. 2(c)].

The dispersion model of the silicon nitride film uses a new amorphous dispersion relationship that is derived on the basis of the Forouhi-Bloomer formulation with tabulated optical constants.²⁶ The refractive index is about 2 at 632.8 nm, which is in agreement with the literature for thin LPCVD nitride films.²⁷ The salt layer is fitted with the Cauchy absorbent dispersion law coupled with a void simulation (Cauchy Transparent) to take into account the porosity of the salt layer. The fitting procedure results in the following salt dispersion law that is fixed for all the experiments:

$$\text{Salt model: } \left\{ n(\lambda) = A + \frac{B \times 10^4}{\lambda^2} + \frac{C \times 10^9}{\lambda^4} ; k(\lambda) = D \times 10^{-5} + \frac{E \times 10^4}{\lambda^2} + \frac{F \times 10^9}{\lambda^4} \right\} + \text{void.}$$

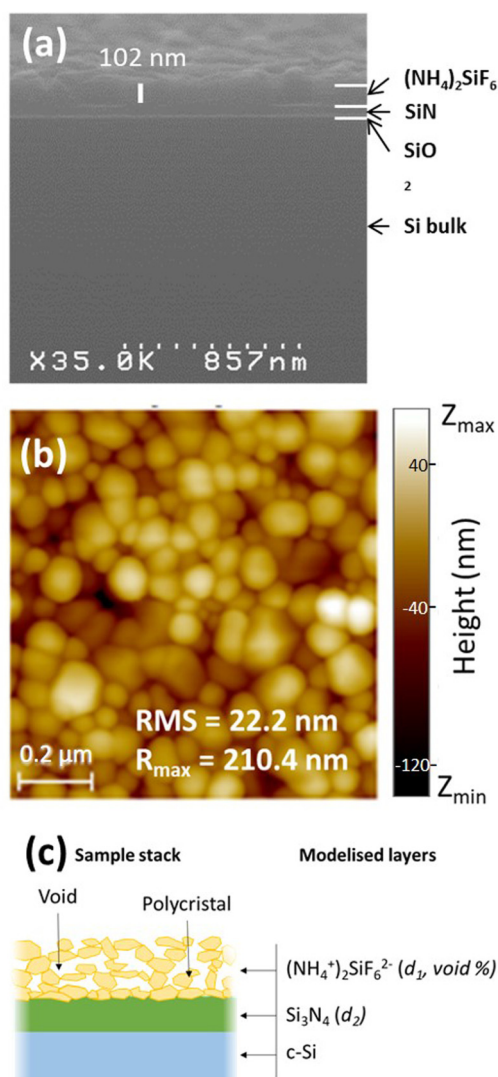


FIG. 2. (a) SEM image and (b) AFM image of the ammonium salt layer formed on Si_3N_4 film exposed to $\text{NH}_3/\text{NF}_3/\text{He}$ remote plasma at 60°C . (c) Schematic of the bilayer model used to fit the ellipsometric data of Si_3N_4 films exposed to NH_3/NF_3 RP process. Free fitting parameters are the thicknesses of the salt (d_1) and Si_3N_4 (d_2) layers, as well as the salt porosity (void %).

After the fitting procedure, the following values were found for the coefficients of the salt dispersion law: $A = 3.53$; $B = E = 0$; $C = 0.47$; $D = 10$; and $F = 0.17$.

This model was used to describe the etching kinetics of Si_3N_4 films exposed to the NH_3/NF_3 RPS process conditions used in this study (wafer temperature of 100°C and a chamber pressure of 2.5 Torr). Indeed, in these conditions, the salt layer is formed during the Si_3N_4 etching, but it outgasses in the chamber at the end of the process during the pump down to reach base pressure (<1 mTorr) (which is not the case at 60°C), preventing from *ex situ* analyses (cf. Sec. III B 2). This is why the ellipsometric model was

developed for the RP process operating at 60°C but was then implemented for the monitoring of Si_3N_4 etching in NH_3/NF_3 RP at 100°C . For the fitting of the kinetic data, the dispersion laws of the unmodified Si_3N_4 and the salt layers are fixed. Only the layer thicknesses and the salt porosity can be varied.

However, we noticed that the porosity was almost constant during the process and comprised between 77% and 82%.

III. RESULTS AND DISCUSSION

A. Characterization of Si_3N_4 films after implantation

In Sec. III A, the Si_3N_4 wafers are exposed to H_2 or He implantations using the plasma conditions given in Table I.

XRR is first used to determine the thickness of the modified Si_3N_4 by implantation.

The XRR measurement of a pristine Si_3N_4 film before implantation is fitted with a bilayer [cf. Fig. 3(a): a 1.1 nm-thick native Si_3N_4 oxide layer with a density of 2.5 g cm^{-3} over a 53.2 nm-thick Si_3N_4 with a density of 3.0 g cm^{-3}]. After implantation, our first approach was to fit the XRR data with a bilayer: a first top layer corresponding to the Si_3N_4 layer modified by the implantation over an unmodified Si_3N_4 layer [cf. Fig. 3(b)]. In the case of H_2 implantation, the fitting procedure indicates that a 5.8 nm-thick modified layer with a density of 2.3 g cm^{-3} lower than the pristine Si_3N_4 is formed at the surface of the unmodified Si_3N_4 layer. However, with this bilayer model, the fit curve derives from the experimental data points for high angles of incidence ($\theta > 1.8^\circ$). Figure 3(c) shows that a fitting procedure using a trilayer model offers a better match with the experimental data with a decrease of the sum of squared error from 0.231 to 0.168. The trilayer model leads globally to the same conclusion as the bilayer one: the H_2 implantation using the plasma conditions of Table I results in a total modified 5.8 nm thick Si_3N_4 layer having a lower density than the pristine Si_3N_4 and does not introduce significant sputtering or swelling (since the total Si_3N_4 thickness before and after implantation for both models is around 54.0 ± 0.5 nm). However, the trilayer model suggests that a thin layer (of about 1 nm thick) with an even lower density (2 g cm^{-3}) is formed at the very top surface (<1 nm). This cannot be attributed to surface roughness generation during implantation since AFM measurements performed before and after implantation show almost similar RMS roughness of 0.26 nm and 0.43 nm, respectively (not shown here). Similar findings are made with He implantation. The fitting procedure using the trilayer model shown in Fig. 3(d) indicates that He implantation using the plasma conditions of Table I results in a total modified 4 nm thick Si_3N_4 layer composed of a thin and low density top modified layer ($0.8\text{ nm}/1.2\text{ g cm}^{-3}$) and an underneath intermediate modified layer ($3.2\text{ nm}/2.6\text{ g cm}^{-3}$). No sputtering or swelling is also measured.

It is noticed that for similar ion energy, the implanted depth is higher for H_2 than He implantation since smaller H^+ ions penetrate deeper into materials.¹⁴ Moreover, the density decrease induced by the implantation is much important after H_2 (25%) than He (12%) implantation. This density decrease had already been predicted by molecular dynamics simulations performed by Martirosyan *et al.*²¹ In their study, they estimated a density decrease of 7% of the modified Si_3N_4 by He implantation using 50 eV ion energy.

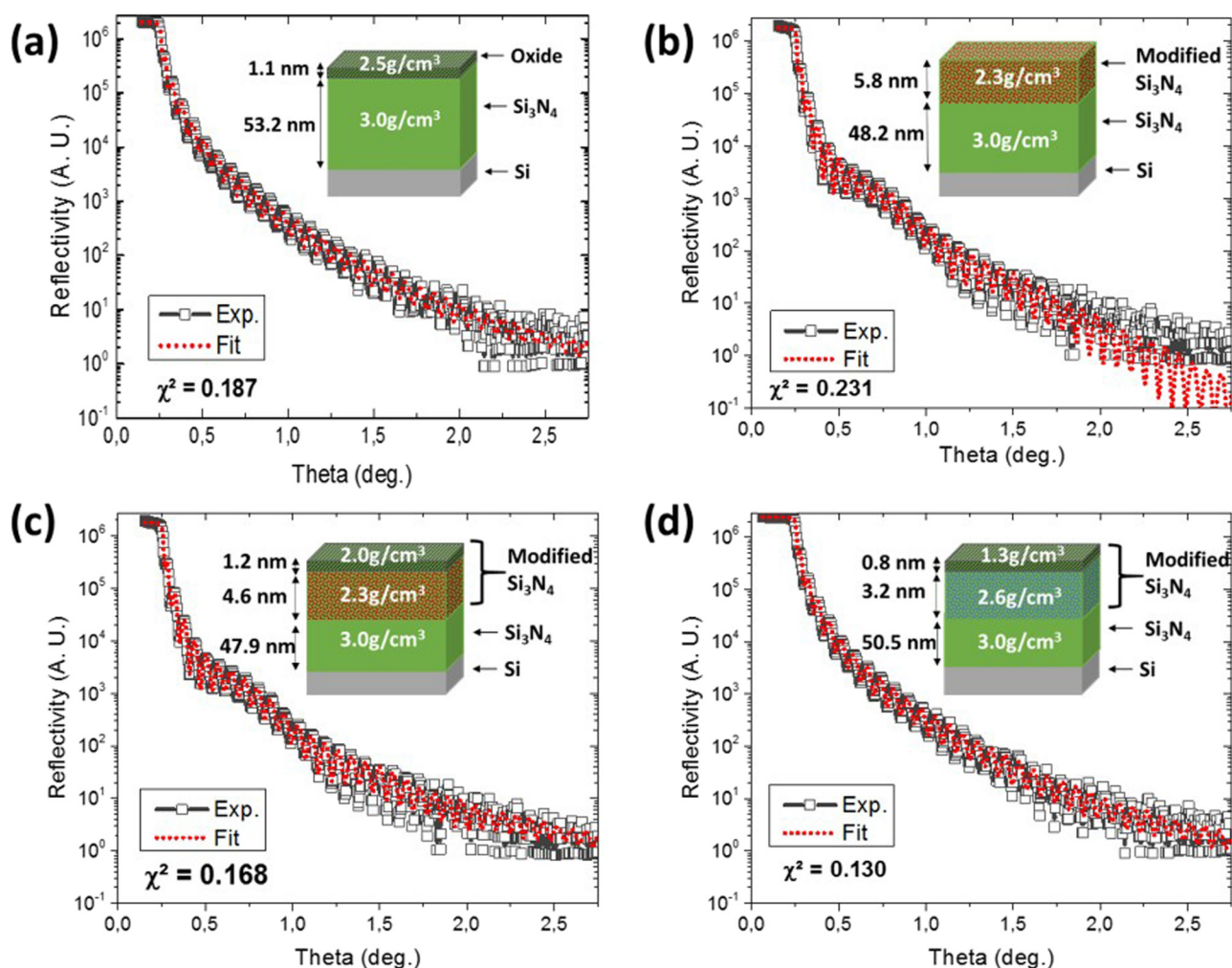


FIG. 3. XRR experimental data (black open squares) and fitting curve (dot red line) of (a) pristine Si_3N_4 film, (b) Si_3N_4 film after H_2 implantation using a bilayer model for the fit, (c) Si_3N_4 film after H_2 implantation using a trilayer model for the fit, and (d) Si_3N_4 film after He implantation using a trilayer model for the fit.

To consolidate these results, the total modified thicknesses were compared to the profiles given by the Monte Carlo code Stopping and Range of Ions in Matters (SRIM) developed by Ziegler.²⁸ For our simulations, the substrate had a thickness of 54 nm and a density of 3.0 g cm^{-3} in accordance with the XRR characterization of the pristine LPCVD silicon nitride film. We estimated the simulated thickness of the implanted layer by summing the mean projected range (R_p) and the square root of the variance. The penetration depth calculated with SRIM simulation are 5.6 nm and 3.3 nm for hydrogen and helium, respectively. These values are very close to the experimental modified thickness determined by XRR (5.8 nm after H_2 implantation and 4 nm after He implantation) confirming that the modified thickness corresponds indeed to the depth at which H^+ or He ions can penetrate into the Si_3N_4 material with the used ion energy.

Quasi *in situ* ARXPS analyses have also been carried out after He and H_2 implantations. Prior to the implantation, the Si_3N_4

films are deoxidized with an HF bath. Three chemical elements are detected: Si, N, and O. He and H cannot be detected by XPS in present. Thanks to the angular resolution of our spectrometer, the depth profiles of oxygen atomic concentration for HF-deoxidized Si_3N_4 films before and after He or H_2 implantation can be reconstructed as shown in Fig. 4. The depth profiles for pristine Si_3N_4 with its native oxide are also represented for comparison. Figure 4 confirms the efficiency of HF wet etchant to deoxidize the Si_3N_4 (even though some O traces remain). After implantation, the amount of O at the very near surface is clearly increased and is detected within the first nanometer of the surface. As XPS analyses are achieved in a quasi *in situ* way, it is likely that this oxygen comes from the Y_2O_3 reactor wall or residual oxygen in the chamber. The oxidation of InGaAs after He implantation has also been observed in relatively similar conditions by Bizouerne and co-workers.²⁹ They explained that if contaminants are present in

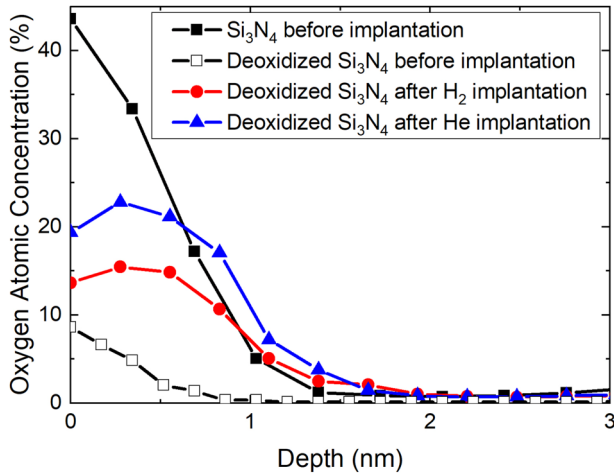


FIG. 4. ARXPS depth profile of the oxygen atomic concentration of HF-deoxidized Si₃N₄ films before (black empty square) and after hydrogen (red circle) and helium (blue triangle) implantations compared to the one of pristine Si₃N₄ with its native oxide (full black square).

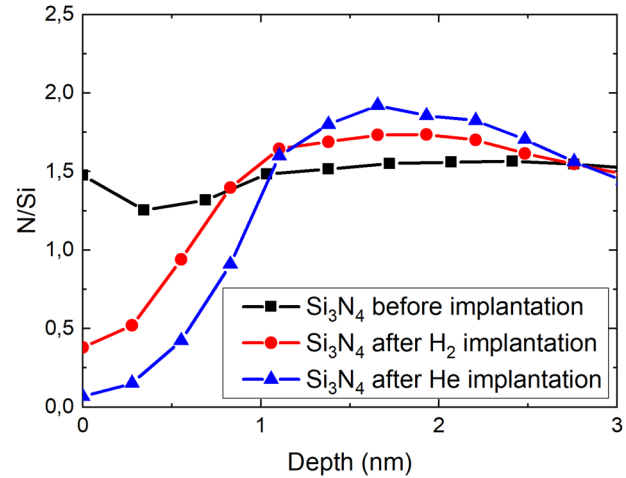


FIG. 5. N/Si atomic ratio as a function of the depth probed by ARXPS of deoxidized Si₃N₄ film before (black square) and after H₂ (red circle) and He (blue triangle) implantations.

the He gas phase, they will be more likely ionized compared to helium because their ionization potential is much lower than the one of helium (He: 24.59 eV and O: 13.62 eV) and will also be implanted.³⁰ The amount of oxygen is higher after He than H₂ implantation, but we noticed that the amount of implanted O is very dependent on the reactor wall conditioning and no conclusion can be drawn on which between He or H implantation brings more contaminants. We suspect that this thin layer rich in O contaminants corresponds to the top surface layer detected by XRR.

Besides highlighting the presence of oxygen at the Si₃N₄ surface, ARXPS analyses also allowed us to estimate the stoichiometry of the silicon nitride film after the implantation. Figure 5 shows the N/Si atomic ratio as a function of the probed depth for implanted and nonimplanted Si₃N₄ films. For the pristine Si₃N₄ sample, the N/Si ratio is almost constant on the probed depth and is equal to 1.5, which is slightly higher than the expected theoretical ratio of 1.33 for stoichiometric Si₃N₄. After both He and H₂ implantations, a nitrogen depletion is observed at the very top surface (within the first nanometer) and a nitrogen enrichment below at 1–3 nm depth. Finally, the Si₃N₄ film tends to recover its initial stoichiometry at about 3 nm of depth. This trend is fully consistent with the prediction of the molecular dynamics simulations by Martirosyan *et al.*²¹ They predict that the He ion implantation into Si₃N₄ films leads to a rearrangement of the bonds. The Si–N bonds are broken in all the modified volume and are accompanied by the formation of Si–Si bonds within the first nanometer and the formation of N–N bonds just below. The nitrogen depletion of the near surface is mostly attributed to the preferential sputtering of nitrogen atoms compared to that of silicon atoms due to the more efficient collisional energy transfer between N–He compared to Si–He. In our case, we do not see the formation of Si–Si bonds at the very near surface, but instead see Si–O bonds. Indeed, molecular dynamics simulations do not take into account the presence of

oxygen contaminants during the implantation. It is likely that Si–O bonds are more likely formed than Si–Si bonds following the cleavage of the Si₃N₄ bond during the He implantation.

Ex situ ToF-SIMS analyses were carried out after He and H₂ implantations. Unfortunately, He could not be detected by ToF-SIMS because no detectable secondary ions could be formed due to its high ionization energy. The ToF-SIMS experiments obtained after He implantation do not bring any complementary information and are thus not shown here. The hydrogen and oxygen in-depth distributions obtained on H₂ implanted Si₃N₄ films by ToF-SIMS are represented in Fig. 6.

The simplest formula for expressing an implantation profile is a Gaussian distribution. However, real ion implantation profiles are often asymmetric and the symmetric Gaussian function cannot model the tail of the distribution. Several models have been proposed to take into account this tail and get an accurate implantation profile reconstruction including the addition of an exponential tail function³¹ or the use of a joined half-Gaussian.³²

In our case, the presence of a positive skew could be attributed to the bimodal distribution of ion energy in the CCP discharge that leads to the fit of two half-Gaussians.³³

The ToF-SIMS profiles of Fig. 6 have been fitted using a probability distribution based on two half-Gaussian distributions as proposed by Gibbons *et al.* [cf. Eq. (1)],³²

$$n(x) = \begin{cases} \sqrt{\frac{2}{\pi}} \frac{\Phi}{(\sigma_{pf} + \sigma_{pb})} \exp\left[-\frac{(x - R_{pm})^2}{2\sigma_{pf}^2}\right] & \text{for } x \leq R_{pm}, \\ \sqrt{\frac{2}{\pi}} \frac{\Phi}{(\sigma_{pf} + \sigma_{pb})} \exp\left[-\frac{(x - R_{pm})^2}{2\sigma_{pb}^2}\right] & \text{for } x > R_{pm}, \end{cases} \quad (1)$$

where $n(x)$ represents the concentration, Φ is the ion dose per unit, R_{pm} is the projected range, σ_{pf} is the standard deviation of the

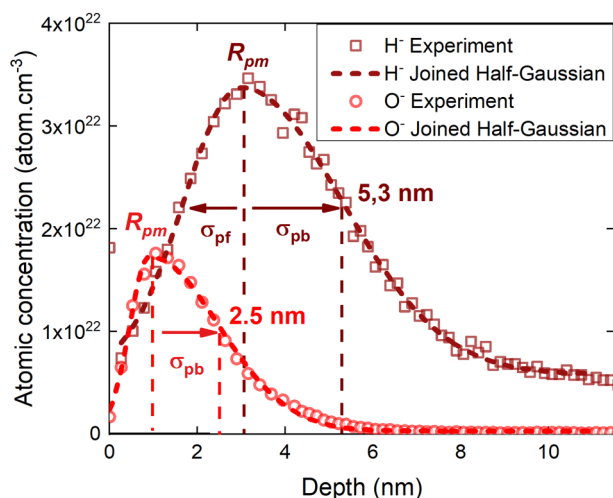


FIG. 6. In-depth H^- (empty purple square) and O^- (empty red circle) distribution in a Si_3N_4 film after H_2 implantation (ToF-SIMS, $\text{Cs}^+/500$ eV) fitted with a two half-Gaussian model.

Gaussian profile between R_{pm} and the surface, and σ_{pf} is the standard deviation of the Gaussian profile below R_{pm} . The values found for the parameters Φ , R_{pm} , σ_{pf} , and σ_{pb} for the O and H depth profiles are represented in Table II.

The agreement between the experimental and fitting data confirms that the ToF-SIMS O and H profiles correspond to those of the implanted species. The penetration depth is estimated to be of $R_{pm} + \sigma_{pb}$, namely, 2.5 nm and 5.3 nm for O and H, respectively.

The O penetration depth estimated by ToF-SIMS is more important than the thickness of the top modified surface layer detected by XRR [only of 1.1 nm, cf. Fig. 3(c)]. We assume that the XRR technique is not robust enough to discriminate the thickness of the two layers presenting gradients in the concentration and having close densities. On the contrary, the depth at which H penetrates into the Si_3N_4 film deduced from the model is quite consistent with the total modified layer estimated by XRR [of 5.8 nm, cf. Fig. 3(c)]. Experimentally, using infrared characterizations, Posseme *et al.*¹⁷ found that the implanted H forms NH and SiH bonds. More precisely, the dynamic molecular simulation of Martirosyan³⁴ of H_2 implantation of Si_3N_4 films reveal that SiH_3 bonds are mainly formed at the H peak maximum concentration, while SiH_2 dominates in the rest of the modified layer followed by SiH and then NH.

To summarize this part, we have seen that He or H_2 implantation can chemically modify the first nanometers of the Si_3N_4

TABLE II. Values of the parameters of the two half-Gaussian equations used to fit the O^- and H^- profiles [cf. Eq. (1)].

	R_{pm} (nm)	σ_{pf} (nm)	σ_{pb} (nm)	Φ (at nm^{-1})
O^-	0.9	0.4	1.6	2.7×10^{27}
H^-	3.0	1.3	2.3	8×10^{22}

surface. With ion energies of 120 eV and 130 eV being used for He and H_2 implantation, respectively, Si_3N_4 is modified on the first 4.0 and 5.8 nm, respectively, consistently with SRIM simulations. In both cases, the modified layer consists of a bilayer: a near surface layer of about 1–2 nm thick with a low density (of 2 g cm^{-3} and 1.3 g cm^{-3} for hydrogen and helium implantation, respectively), depleted in nitrogen and rich in oxygen contaminants, and a disorganized sublayer with lower density than the pristine Si_3N_4 (about $2.3\text{--}2.6 \text{ g cm}^{-3}$) and slightly richer in nitrogen than the pristine materials (certainly via the formation of N–N bonds). In the case of H_2 implantation, it is possible to detect the presence of H in the Si_3N_4 material after implantation over the entire depth of the modified layer thickness using the ToF-SIMS analyses.

From molecular dynamics simulations,²¹ it is also suspected that He is present in the modified layer of the He-implanted Si_3N_4 , although we could not prove it experimentally. Finally, we systematically observe the implantation of oxygen contaminants at the very near Si_3N_4 surface after both He and H_2 , which could not be predicted by the molecular dynamics simulation and may play a role in the RP etching mechanisms as described in Sec. III B.

B. Etching kinetics of Si_3N_4 films in $\text{NH}_3/\text{NF}_3/\text{He}$ remote plasma

In Sec. III B, pristine and implanted Si_3N_4 wafers are exposed to the 400 sccm $\text{NH}_3/40$ sccm $\text{NF}_3/1400$ sccm He remote plasma using 250 W as the source power and 2.5 Torr as the pressure chamber

1. Pristine Si_3N_4

The etching kinetics of pristine Si_3N_4 films exposed to $\text{NH}_3/\text{NF}_3/\text{He}$ remote plasma at 100°C have been investigated by real-time ellipsometry. As already mentioned, the etching proceeds with the formation of an ammonium salt layer on the surface. The plasma reactive species absorb on the surface, react with Si_3N_4 , and turn Si_3N_4 into a salt. Similar to silicon oxidation mechanisms, the salt formation leads to Si_3N_4 consumption. For each processing time, the kinetic data are fitted with a bilayer composed of a salt layer over an unmodified Si_3N_4 layer, with the dispersion law described in Sec. II C 4.

Figure 7(a) compares the consumed thickness of the pristine Si_3N_4 film with its native oxide and the Si_3N_4 film deoxidized with a 1% HF wet etchant when exposed to the $\text{NH}_3/\text{NF}_3/\text{He}$ RP. For the deoxidized sample, no salt formation is detected even after a very long processing time of 1000 s, as well as no Si_3N_4 consumption. For the pristine Si_3N_4 , an etch delay of about 70 s is observed before the etching starts. We assume that this delay corresponds to the time needed for the reactive neutrals of the remote plasma to adsorb on the surface and then react with the substrate. This preliminary observation tends to suggest that the surface oxidation state plays a key role in the etching mechanisms and that oxygen acts as a reaction catalyst. After this incubation time, a salt layer starts to grow causing the Si_3N_4 consumption. Figure 7(b) shows that there is a linear relation between the salt layer thickness and the consumed Si_3N_4 thickness, with a correlation coefficient of 6.1. Other experiments not shown here indicate that this coefficient depends on the nature of the etched material but also on the

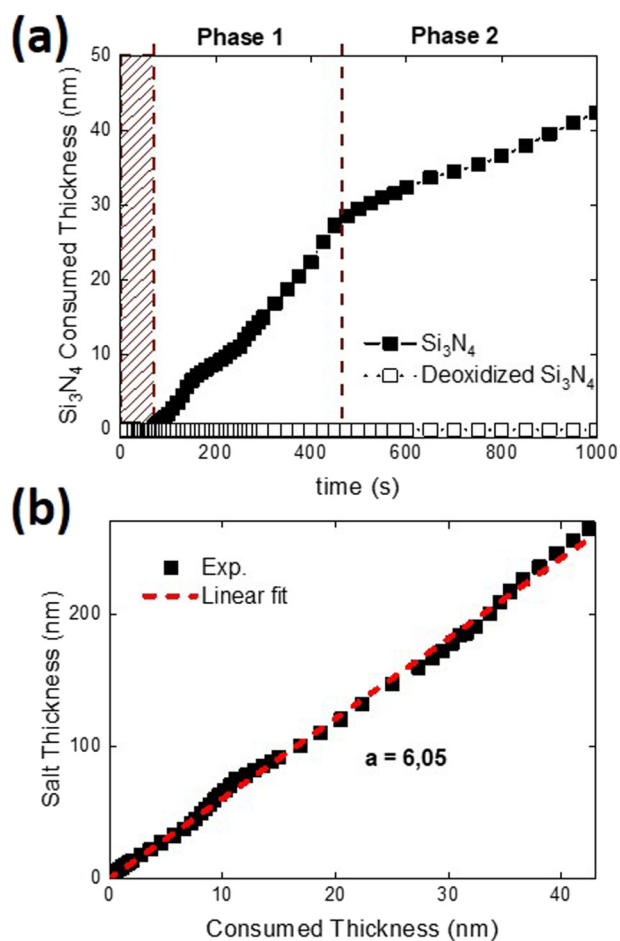


FIG. 7. (a) Etching kinetics of HF-deoxidized (empty black square) and pristine (full black square) Si_3N_4 in $\text{NH}_3/\text{NF}_3/\text{He}$ remote plasma at 100°C . (b) Salt thickness as a function of the consumed Si_3N_4 thickness.

substrate temperature and the NH_3/NF_3 ratio introduced in the remote plasma gas phase (this will be discussed in another publication). This reaction mechanism implies that the Si_3N_4 layer is constantly consumed with a growing salt layer upon its surface.

As shown in Fig. 7(a), the Si_3N_4 consumption is not linear with time and slows down with a longer exposure time (here above 475 s). This indicates that above a certain salt thickness on the Si_3N_4 film (here of 166.7 nm corresponding to 28.6 nm of etched Si_3N_4 after 475 s of RP), the Si_3N_4 consumption is limited by the reactive neutral diffusion through the salt layer until the salt/ Si_3N_4 interface. It is also interesting to highlight that the etching of the pristine Si_3N_4 is not limited to the depth at which it is oxidized (about 2 nm), meaning that once the salts are formed, fluorine and hydrogen present in the salt can diffuse through the interface and consume Si_3N_4 while the plasma still supplies the salt layer with reactive species. Once the RP is turned off (at the end of the experiment), the pressure in the chamber is decreased down to the

chamber base pressure (<1 mTorr), while the wafer is still at the process temperature of 100°C . During this step, the ammonium salts are outgassed leaving a clean surface without any fluorinated ammonium residues. To illustrate and demonstrate this point, two experiments have been performed (cf. Fig. 8). The first experiment consists of exposing the pristine Si_3N_4 to the $\text{NH}_3/\text{NF}_3/\text{He}$ RP process at 2.5 Torr for 150 s (stage 1); then, the plasma is turned off and the gas is evacuated to decrease the pressure down to the chamber base pressure while the wafer is still maintained at 100°C (stage 2, 170 s); finally, the RP process at 2.5 Torr is turned on again during 150 s (stage 3). The second experiment is similar except for the second stage. Instead of evacuating the reactive gas,

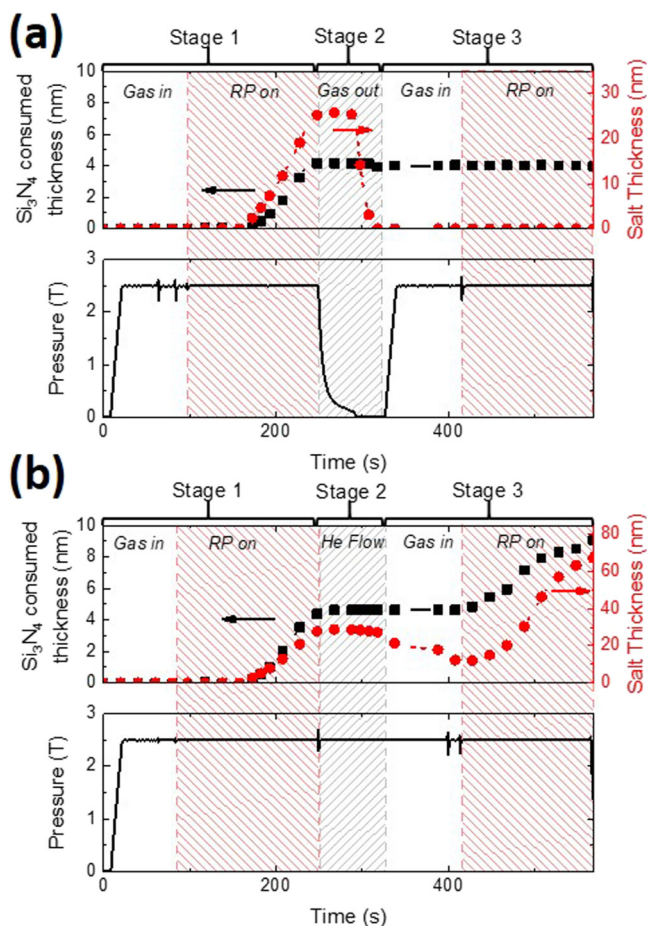


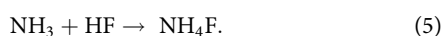
FIG. 8. Kinetics of the pristine Si_3N_4 film consumption (black square) and salt formation (red circle) during a three-stage process. Stages 1 and 3 are similar and correspond to the $\text{NH}_3/\text{NF}_3/\text{He}$ RP process at 2.5 Torr comprising a stabilization step where the gas are introduced and the pressure in the chamber increases up to the operating pressure (Gas in—white area), followed by the RP source ON step (red dashed area). Stage 2 (dark dashed dark area) corresponds to (a) a Gas phase evacuation step and (b) a He stabilization step at 2.5 Torr. For both (a) and (b), the pressure in the reactor is also presented (black line) along with the wafer temperature.

the He flow is supplied to maintain the chamber pressure at 2.5 Torr.

During the first RP on stage, Si_3N_4 is etched as expected through the growth of a salt layer for both experiments. The salt layer reaches a thickness of 25.8 nm for an Si_3N_4 consumed thickness of 4.2 nm. However, during the second stage, Fig. 8 shows that the salt layer desorbs almost instantly as the chamber pressure decreases below 10 mT in experiment 1, while it remains on the substrate if the chamber pressure is kept constant at 2.5 Torr in experiment 2. This means that in experiment 1, the pressure in stage 2 decreases below the saturation vapor pressure of the salt at 100 °C, allowing the salt to desorb. Moreover, during the second RP on stage (stage 3), no salt growth and consequently no Si_3N_4 etching is observed in experiment 1, while Si_3N_4 etching proceeds normally with the formation of the salt layer in experiment 2 without incubation time. Those two experiments highlight two phenomena. First, experiment 1 confirms the trend of Fig. 7(a) that the Si_3N_4 surface oxidation state plays a role in the etching reaction ignition since the Si_3N_4 surface is oxidized at the beginning of the first RP on stage and deoxidized at the beginning of the second RP on stage. Secondly, experiment 2 shows that if a salt layer remains on the Si_3N_4 surface when the RP is turned off and on, the reaction goes on as if there was no interruption since the 70 s incubation time of stage 1 is not observed during stage 3. This suggests that the deposited film contains some etching species for the Si_3N_4 film.

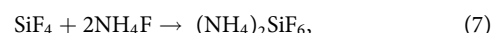
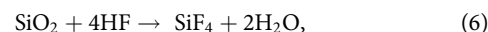
2. Discussion on the etching mechanisms of Si_3N_4 films exposed to NH_3/NF_3 remote plasma

In the literature, a reaction scheme has been proposed for the etching of SiO_2 films exposed to NF_3/NH_3 or NF_3/H_2 remote plasma, but very little has been reported for Si_3N_4 . It is suggested that NH_4F and HF reactants are formed in the NH_3/NF_3 remote plasma chamber by NF_3 (respectively NH_3) dissociation into NF_x ($x = 1-2$) and F [respectively NH_x ($x = 1-2$) and H] and subsequent recombination of these fragments together and with the feed gases, as described by Eqs. (2)–(5),^{17,23–25}



Because of the high electronegativity of the F atom, F in the NH_4F and HF molecules is negatively charged while NH_4 and H are positively charged. Similarly, O and Si of SiO_2 are negatively and positively charged, respectively. F will then preferentially attack positively charged Si atoms while H and NH_4 are attracted to O through a Coulomb force. These interactions weaken both Si–O and H–F bonds and results in Si–F bond formation. The released negatively charged oxygen atoms combine with H to generate H_2O [cf. Eq. (6)]. The resultant etching products, such as SiF_4 , react with NH_4F and change into the final product $(\text{NH}_4)_2\text{SiF}_6$ as described by Eqs. (6)–(8).^{17,18,24,25} Hayashi *et al.*³⁵ suggests that the

reactants are adsorbed on the wafer surface, on which a condensed phase is formed, so that a type of ammonium fluoride etching in the liquid phase takes place,



In the case of Si_3N_4 , Knolle and Huttemann observed that the formation of a $(\text{NH}_4)_2\text{SiF}_6$ layer (and thus the etching of the Si_3N_4 film) when exposed to a CF_4 plasma (remote ICP) occurs only if its surface is hydrogenated and oxidized.³⁶ This suggests that the presence of SiO bonds favor the chemical reaction.

It is also interesting to note that the etching of pristine Si_3N_4 films exposed to the NH_3/NF_3 remote plasma at 2.5 Torr drastically slows down with increasing temperature and even stops above 120 °C (cf. Fig. 9). This etch trend with temperature is quite unusual for a pure chemical type of etching that generally displays an Arrhenius dependence on the temperature.³⁷ On the contrary, the temperature dependence observed is well consistent with the theory of chemisorption kinetics.³⁸ As theoretically or experimentally reported,^{38,39} when gaseous molecules or atoms collide with a surface, they may first adsorb on the surface in a physisorbed precursor state, which acts as a reservoir for the subsequent adsorption into a chemisorbed state. The fraction of the impinging molecules that is finally chemisorbed results from the competition between two processes: the incorporation of physically adsorbed molecules into a chemisorbed layer, on the one hand, and their evaporation into the surrounding gas, on the other hand. The dependence of the chemisorption rate on the temperature is determined by the difference in the activation energy of these two processes. In our case, it is likely that the activation barrier for the desorption of

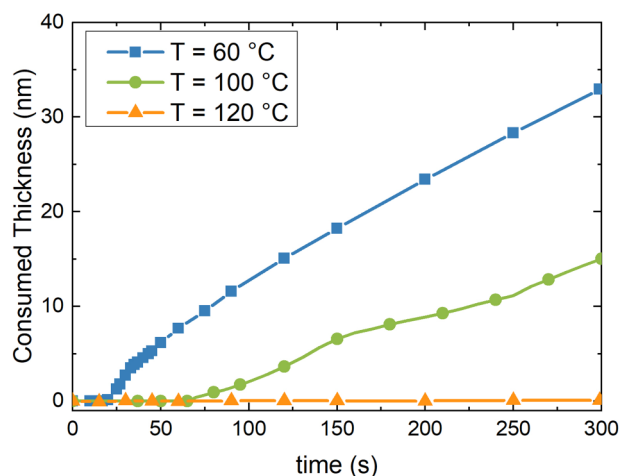


FIG. 9. Etching kinetics of Si_3N_4 film at 60 (blue square), 100 (green circle), and 120 °C (orange triangle) in $\text{He}/\text{NH}_3/\text{NF}_3$ plasma.

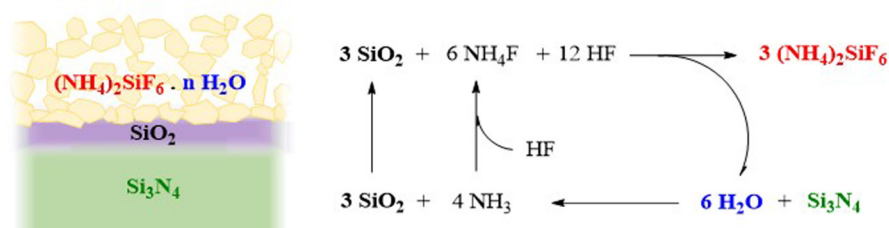
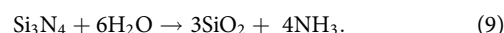


FIG. 10. Reaction path of Si_3N_4 etching in NH_3/NF_3 remote plasma.

NH_4F and HF reactants is greater than the one of their chemisorption, implying that a rise in temperature rapidly leads in a depopulation of the physisorbed layer that cannot be compensated by the enhanced chemisorption with temperature. This results in an increase of the incubation period and a decrease of the etch rate with increasing temperature (cf. Fig. 9).

The etch kinetics of pristine and HF -deoxidized Si_3N_4 at the given process temperature of 100°C shown in Fig. 7 clearly indicates that the adsorption step is the rate limiting step of the reaction and suggests that the presence of Si-O rather than Si-N bonds lowers the activation barrier for the dissociative chemisorption. In a pure chemical process, etch rates are determined by the chemical bond strength that holds the material together. The rate-determining step is then the breaking of the first Si-N bond (or more precisely the Si-NH_2 terminated surface) in the case of HF -deoxidized Si_3N_4 or Si-O bond (more precisely the Si-OH terminated surface) and its substitution into Si-F bond. The Si-O bond (799 kJ/mol) is stronger than the Si-N bond (470 kJ/mol), which suggests that the activation barrier for the chemisorption should be higher in the case of a SiO_x surface. In fact, Knotter *et al.* showed that in HF_2^- ($\text{F-H}\cdots\text{F}^-$) environment (equivalent to our $\text{NH}_4^+ \text{F}^- \cdots \text{H-F}$ physisorbed layer), there is a site path for replacing the OH by F in which the Si-OH bond does not have to be broken first.^{40,41} This path lowers the activation barrier of the chemisorption step compared to the case of SiN system in which the Si-N bond needs to be broken first.

This mechanism could explain why the etching starts on the pristine SiN and not on the deoxidized substrate. Moreover, once the etching has started, the water formed upon the reaction of NH_4F and HF with the native SiO_2 present at the surface of the Si_3N_4 [cf. Eq. (8)] remains in the ammonium fluorosilicate layer as a hydrate and can further react with Si_3N_4 underneath to form new SiO bonds [cf. Eq. (9)],



The proposed mechanism is illustrated in Fig. 10. It emphasizes the role of oxygen as a surface oxidant that allows the reaction to be pursued.

However, Knotter *et al.* showed that once the first SiF bond is formed, the activation barrier to break a new adjacent SiN bond is lower because of the stronger polarization of the SiF bond with respect to the SiN bond. The Si center becomes prone to a nucleophile attack by the HF molecule as illustrated in Fig. 11. The SiN bond is broken and replaced by SiF and the nitrogen atom is protonated. This mechanism is repeated three times until forming the reactions products SiF_4 and NH_3 [cf. Eq. (10)]. SiF_4 can further react with NH_4F to form the salt layer [Eq. (11)], the balance equation being given in Eq. (12) as

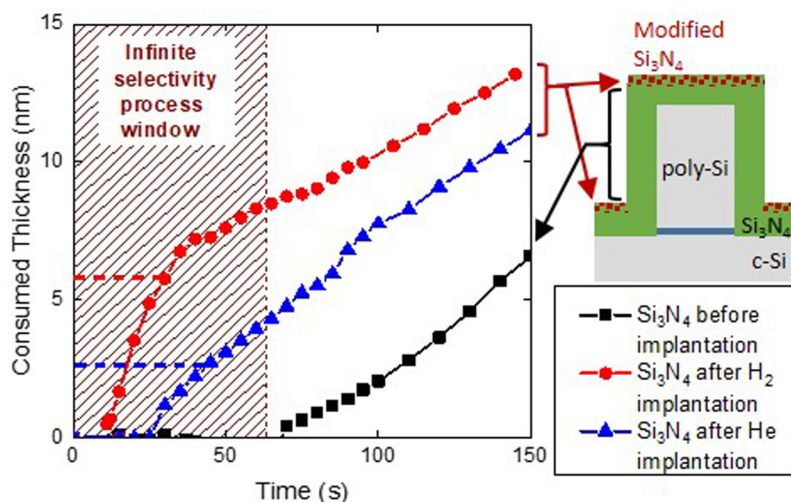
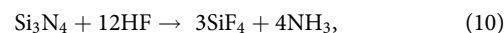
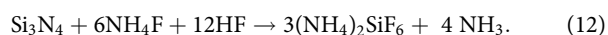
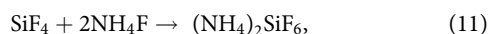


FIG. 11. Schematic representation of a substitution reaction to free the Si-F unit.



3. Implanted vs nonimplanted Si_3N_4

Figure 12 compares the etch kinetics of pristine and implanted Si_3N_4 films when exposed to $\text{NH}_3/\text{NF}_3/\text{He}$ remote plasma process at 100°C . The Si_3N_4 films are HF-deoxidized prior the implantation, while the pristine Si_3N_4 film still has its native oxide. The ellipsometric data of implanted Si_3N_4 are also fitted with a bilayer model using similar salt dispersion law to the one used for the pristine materials. It is observed that the incubation time is considerably reduced for implanted Si_3N_4 films, the etching starting after 11 s and 27 s for H_2 and He implantation, respectively, against 70 s for the pristine Si_3N_4 . It should be noted that the incubation time are reproducible at ± 5 s.

Based on the etching mechanism proposed in Sec. III B 2, we believe that the oxygen incorporated into the Si_3N_4 film by the implantation step acts as a catalyst of the reaction between the plasma reactants and Si_3N_4 . But its presence only cannot explain the lower incubation time observed for H_2 and He implantation compared to the Si_3N_4 film with its native oxide, since the oxygen content at the top surface is higher for pristine Si_3N_4 film (cf. Fig. 4). The disorder introduced by the implantation in the Si_3N_4 films may also play a role. From the XRR measurements, the top oxide layer generated by the implantation is less dense than a native oxide. The dangling bonds and porosity created by the implantation may favor the physisorption and the subsequent chemisorption of the neutral reactive species. We also noticed that for any implantation or RP process conditions, the incubation time is always lower for H_2 implantation than He implantation suggesting that H-terminal bonds could constitute favorable attack sites.

In the He case, once the etch starts, the Si_3N_4 consumed thickness evolves linearly with the processing time and the etch

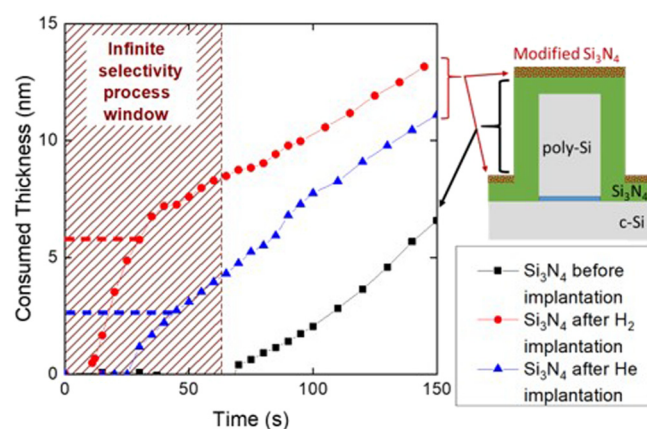


FIG. 12. Etching kinetics of deoxidized Si_3N_4 film after H_2 (red circle) and He (blue triangle) implantation as well as pristine Si_3N_4 film (black square) in $\text{He}/\text{NH}_3/\text{NF}_3$ plasma at 100°C .

kinetics are similar to the ones of the Si_3N_4 pristine film (5.0×10^{-2} nm/s). On the contrary, in the H_2 implantation case, a change of the etch kinetics is observed at the depth corresponding to the modified layer thickness measured by XRR. This transition occurs after a 6 nm etch depth. It is also noticed that once the modified layer is etched, the Si_3N_4 film is etched with similar etch kinetics to the ones of the pristine Si_3N_4 film. The etch kinetics of the modified layer by H_2 implantation (2.9×10^{-1} nm/s) is higher than the ones of the pristine and He-implanted Si_3N_4 films (5.0×10^{-2} nm/s) allowing a selectivity of modified Si_3N_4 after a H_2 implantation over nonmodified Si_3N_4 of 5.8. The higher etch rate for the H_2 implanted Si_3N_4 layer goes along with a slight decrease of the salt porosity (with a void of 75% against 80% for pristine and He damaged Si_3N_4 films) and the correlation coefficient is less important (4.2 vs 6.1). Once the H_2 implanted Si_3N_4 layer is etched, the coefficient and the void percentage of the pristine Si_3N_4 are recovered.

In the steady-state regime, once the etching is initiated, there is in final no etch selectivity between the top modified layer by the He implantation over the pristine Si_3N_4 material, while a low etch selectivity of about 5.8 is expected in the H_2 implantation case. This selectivity is the same as the one of 6 found by Posseme *et al.*¹⁷ for Si_3N_4 removal using NH_3/NF_3 remote plasma, which is not satisfying for the spacer etch process application and is far below the selectivity of 31 achieved using 20% HF gas.^{15,16}

These results suggest that the hydrogen incorporation into the Si_3N_4 film is thermodynamically favorable for the salt formation and thus the Si_3N_4 consumption.

We think the etching mechanisms of implanted Si_3N_4 are similar to the ones illustrated in Fig. 11 and Eqs. (10)–(12). The main difference resides in the number of SiN units to break, which is the rate limiting step. Martirosyan *et al.*³⁴ have shown with their dynamic molecular simulation that the amount of SiN bonds broken by He implantation is lower than for H_2 implantation, which is consistent with the higher density of the modified layer by He implantation predicted by XRR (cf. Fig. 3). The damage generated by the He implantation may not be sufficient to see a significant difference in the etching kinetics compared to the pristine material. It may just activate the etching, thanks to O incorporation and formation of dangling bonds.

On the other side, as mentioned in Sec. III A, H_2 implantation results in the formation of SiH_x and NH bonds, meaning that the Si_3N_4 network is broken with less Si-N units. The SiH_x units present in the H_2 implanted layer are more easily transformed into SiF_x than SiN_x bonds in the pristine materials for thermodynamical reasons. Moreover, some nitrogen atoms are already protonated, which is favorable for the formation of the NH_3 etch by-products.

Finally, Fig. 11 demonstrates that the functionalization of the Si_3N_4 surface by implantation activates the chemical reaction between the Si_3N_4 film and the reactants present in the diffusion chamber and considerably reduces the incubation time. This offers a process window during which the implanted Si_3N_4 is etched with infinite selectivity over the pristine Si_3N_4 , which corresponds to the process duration that is inferior to the pristine Si_3N_4 incubation time (about 70 s). This phenomenon can be exploited in a two-step cycling process comprising implantation and remote plasma etching steps to make topographically selective etching as discussed below in Sec. III C.

C. Two-step cycling etching for topographically selective etching

The current trend in atomic layer deposition (ALD) is to cycle a selective functionalization step and deposition step to make topographically⁴² or chemical⁴³ selective deposition. The concept is based on the fact that the deposition characteristics depend on the surface properties of the employed substrate.⁴⁴ The functionalization step is aimed to chemically and locally modify the surface of one material with respect to the other surfaces in order to inhibit or activate reactive sites and then prevent or catalyze further reactions between the ALD precursor molecules and the functionalized surface. In our case, it happens that remote plasma processes whose etching mechanisms rely on the chemical action of plasma neutrals are also very sensitive to the chemistry of the substrate. The implantation step will functionalize the horizontal surfaces selectively over the vertical surfaces, thanks to the ion anisotropy (cf. Fig. 12). During the subsequent short RP etching step (<70 s), the etching will be activated on horizontal surfaces while vertical surfaces will not be consumed. The two steps will be repeated until etching the desired horizontal surface thickness.

Figure 13(a) shows a 6 cycle etching of blanket Si_3N_4 with its native oxide alternating a 60 s H_2 implantation step followed by a 30 s $\text{NH}_3/\text{NF}_3/\text{He}$ remote plasma at 100 °C. The plasma conditions are the same as the ones described in Sec. II. Note that the CCP step is performed at 50 mTorr, while the RP step at 2.5 Torr, implying that pressure stabilization steps between those two steps are required.

From Fig. 13(a), the Si_3N_4 consumed thickness at each cycle can be estimated, comprising the part coming from the sputtering occurring during the implantation and the part coming from the RP etching [cf. Fig. 13(b)]. It is observed that the total removed thickness at each cycle is reproducible and of $4.5 \text{ nm} \pm 0.5 \text{ nm}$. The thickness removed during the RP step varies slightly from one cycle to another ($\pm 0.5 \text{ nm}$). This variability of the RP step is mainly attributed to the variability of the incubation time ($15 \text{ s} \pm 5 \text{ s}$). Consistent with the results shown in Fig. 3, there is no sputtering during the implantation step of the first cycle, while the subsequent cycles show between 0.5 nm and 1 nm of sputtering during the implantation. Although the salts are outgassed after the RP step, XPS analyses reveal that a rich in fluorine reactive layer (9% of the total atomic concentration) is left on the Si_3N_4 surface after the RP step [cf. Fig. 13(c)]. This layer has a thickness of 0.7 nm and remains constant at each cycle. We suspect that this layer is easily chemically sputtered by H ions during the subsequent implantation explaining why sputtering is observed for all cycles except for the first one.

To simulate what could happen on Si_3N_4 vertical surfaces (spacer sidewalls), a Si_3N_4 film with its native oxide is exposed to cycles of a two-step process comprising an H_2 gas step (using the H_2 implantation conditions except that the source is turned off) followed by the 30 s RP step at 100 °C. Figure 13(a) shows that the Si_3N_4 film exposed to this cycling process is not etched, meaning that in these conditions, 6 cycles of 30 s RP step is not equivalent to 180 s continuous etching RP process [see Fig. 7(a)]. Indeed, the reactive species that adsorb to the Si_3N_4 surface during the 30 s RP step, but have not reacted yet, are outgassed during the next low-

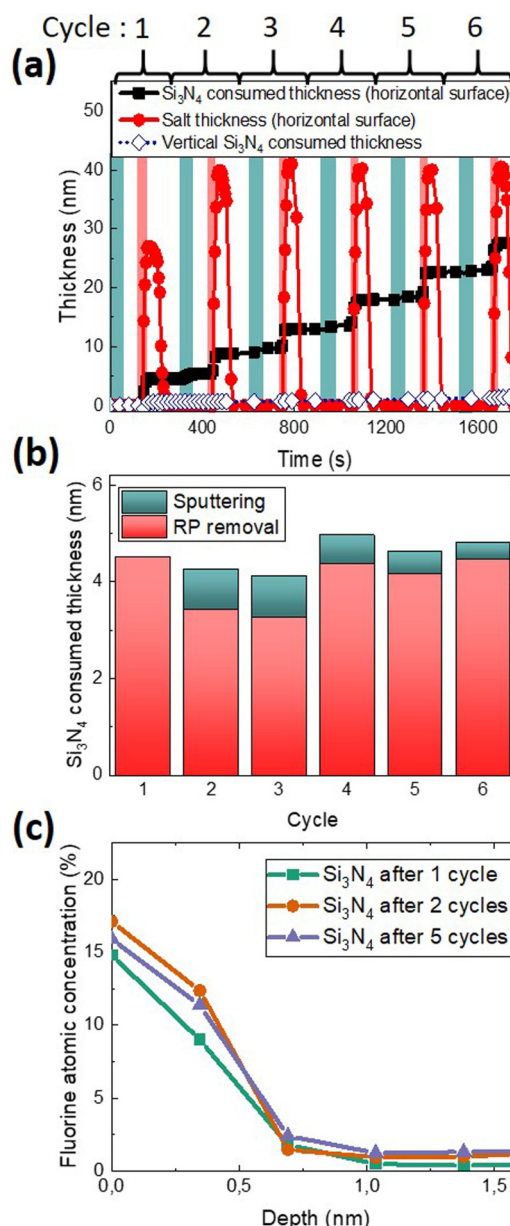


FIG. 13. (a) Si_3N_4 consumed (black square) and salt layer (red circle) thicknesses evolution during a 6 cycle etching alternating 60 s of H_2 implantation and 30 s of $\text{NH}_3/\text{NF}_3/\text{He}$ remote plasma at 100 °C compared to the etch kinetics of a Si_3N_4 film exposed to the alternate of H_2 gas step followed by 30 s of $\text{NH}_3/\text{NF}_3/\text{He}$ remote plasma simulating vertical Si_3N_4 surface (blue empty diamond). (b) Consumed Si_3N_4 thickness per cycle. (c) ARXPS depth profile of the fluorine atomic concentration after 1, 2, and 5 cycles.

pressure gas step. This resets the incubation time of the RP step to zero at each cycle.

It is a promising result for the spacer process application where it is expected that the spacer sidewalls behave similarly.

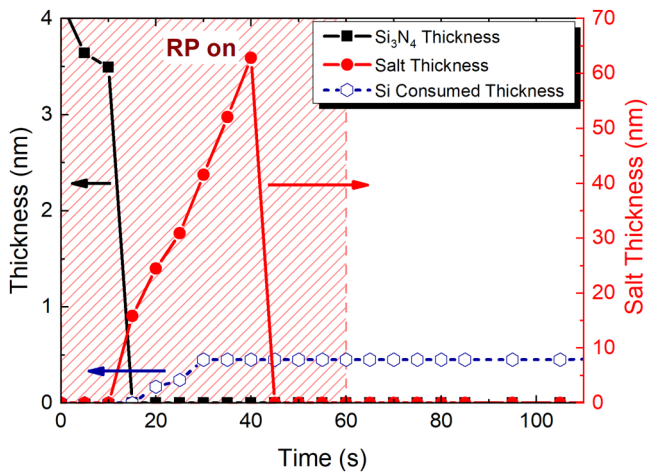


FIG. 14. Si_3N_4 film thickness (black square) vs Si consumed thickness (blue diamond) during the 6th and last cycle that stops on the Si surface. The RP is maintained ON during 60 s containing 45 s of overetch.

However, in the real cycling process, the Si_3N_4 sidewalls are also bombarded by H ions at grazing incidence and reactive H radicals during the implantation. The impact of H radicals can reasonably be neglected since Theджoisworo *et al.*⁴⁵ show that below 150 °C, the etch rate of Si_3N_4 film exposed to H radicals produced by downstream plasma are extremely low (below 0.18 Å/min). On the contrary, the scattering of hydrogen ions produced in the capacitive discharge cannot be ignored. From the work by Donkò *et al.* that investigates the ion properties in low-pressure oxygen CCPs,⁴⁶ it is expected that in the plasma conditions we used for the H_2 implantation (50 mTorr, 120 eV ion energy), most of the ions arrive at angles smaller than 3° meaning that the pattern sidewalls are indeed subjected to ionic bombardment. The ion flux received on the sidewalls may be enough to functionalize the vertical surface and activate its etching without incubation time, which is detrimental for the infinite etch selectivity expected between implanted and nonimplanted Si_3N_4 . However, the ion dose deviated on the sidewalls will be lower than the one received on horizontal surfaces and certainly not sufficient to induce a fully modified H rich layer. Kumakura *et al.*⁴⁷ have shown that the etching rate of the H_2 implanted surface layer depends on the H ion dose. It increases

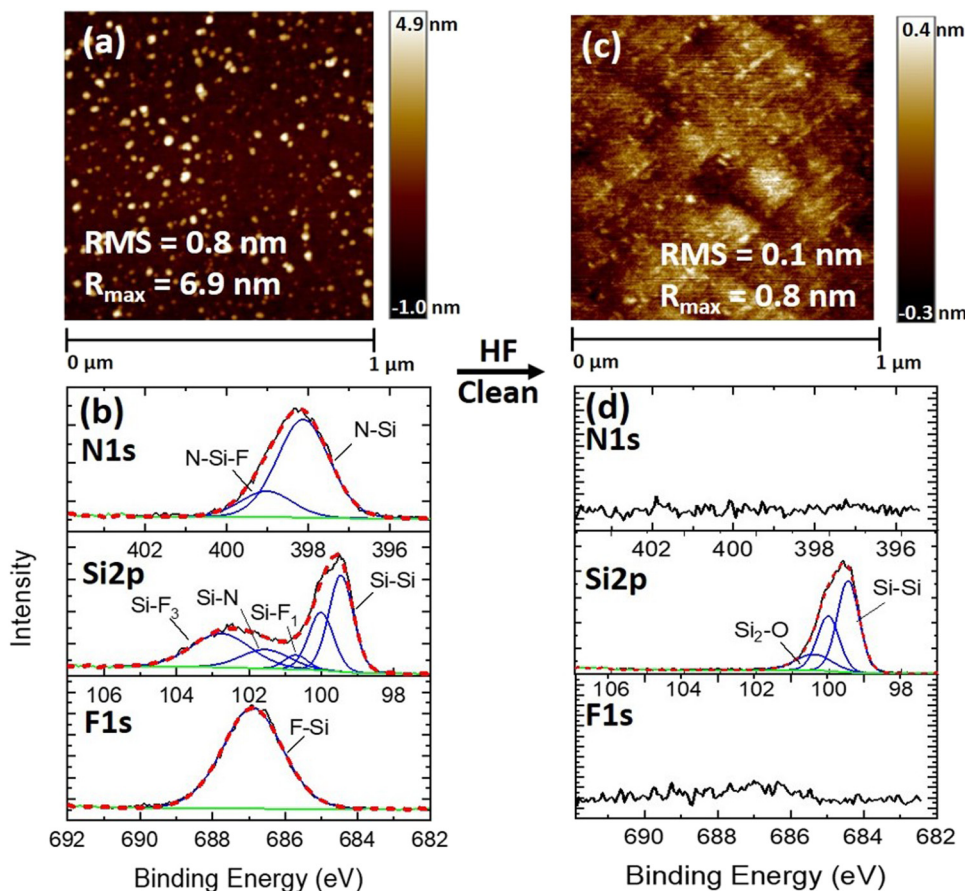


FIG. 15. Surface roughness measured by AFM and XPS spectra of Si surfaces exposed to NH_3/NF_3 RP at 100 °C [(a) and (b)] before and [(c) and (d)] after a HF clean.

with the incorporated H dose until reaching saturation above a certain ion dose threshold. This means that if the etch is activated on the sidewalls, the Si_3N_4 etch kinetics will be lower than on the fully H- modified horizontal surfaces. In such case, it is expected that the etch kinetics of the sidewalls are similar to the He-implanted or pristine Si_3N_4 ones, implying an etch selectivity of only 5.8 between horizontal and vertical surfaces. If this should happen, then the operating conditions of the NH_3/NF_3 remote plasma should be readjusted for higher etch selectivity to be obtained between H_2 implanted Si_3N_4 and pristine Si_3N_4 .

Finally, Fig. 14 shows what happens at the 6th cycle when the Si_3N_4 layer is entirely consumed and the process is stopped on the underneath Si surface. We added 45 s of overetch in the remote plasma to observe the selectivity of the Si_3N_4 film over the underlying silicon. As soon as Si_3N_4 is entirely consumed by the salt formation and the Si surface is reached, the salt layer outgassed and the ellipsometric data indicate that only 0.5 nm of Si is consumed even for very long processing time of RP last step. In fact, this consumption is attributed to the consumption of the native silicon oxide present between the Si_3N_4 and Si layer. AFM and XPS analyses performed on Si surfaces at the end of the 6 cycle process are shown in Fig. 15. The AFM image reveals the presence of some residues on the Si surface that are identified by XPS as salt residues or Si_3N_4 residues [cf. Figs. 15(a) and 15(b)]. Indeed, the Si2p peak is decomposed with 4 contributions: a peak at 99.4 eV attributed to Si-Si bonds, a peak at 101.7 eV attributed to Si-N bonds, and two peaks at 100.7 eV and 102.7 eV attributed to SiF_1 and SiF_3 bonds. The latter are confirmed by the presence of Si-F and N-F bonds on the N1s and F1s spectra. On the F1s spectra, Si-F bond contributions are detected at 687.8 eV. Concerning the N1s spectra, two contributions are detected: N-Si bonds at 397.5 eV and N-F_x bonds at higher energy (398.6 eV).

However, after a 1% HF wet, the Si surface is as clean as an unprocessed Si wafer. The RMS is very smooth of 0.1 nm and with a R_{max} of 0.8 nm, even compared to the RMS of a pristine SOI wafer that is of 0.3 nm with a R_{max} of 2.2 nm. The residues are also all removed as shown by the XPS spectra of Fig. 15(d). We, however, noticed the presence of a new peak on the Si2p spectra at 100.3 eV that we attributed to Si_2O contribution.⁴⁸ This very small oxidation of the Si surface certainly occurred during the transfer from the HF treatment tool to the ARXPS analysis chamber. The presence of carbon contamination, that is considered to generate defects during epitaxial silicon film growth,⁴⁹ was not yet detected.

Those results prove that the cycling process offers infinite selectivity over Si and is free of damage, which is a mandatory criterion for the spacer etch application. Moreover, the etch process and the etch stop can be accurately monitored by kinetic ellipsometry.

IV. SUMMARY AND CONCLUSIONS

Etch selectivity is today a key issue to be addressed in the patterning of complex 2D and 3D MOS stacks. The smart etch concept, which is a two-step process combining implantation and removal steps was initially proposed as a method to etch very thin layers with high selectivity. Although promising, the initial proof of

concept lacks flexibility because of the use of two separate equipment to achieve the two steps of the process. In this article, we propose a new way to implement the smart etch process, by cycling the two steps of the process in the same plasma reactor chamber, which has the capability to produce both a CCP discharge for the implantation step and a remote plasma discharge for the removal step.

We demonstrate that by cycling the two-step process, it is possible to make a topographically selective etching. The key to success of the concept lies in the existence of an incubation period in the RP process that can be tuned by functionalizing the surface state with a treatment. The use of plasma implantation, as a treatment step allows us to selectively modify the horizontal surfaces of the material with respect to the vertical surfaces, thanks to the ion directionality, and makes possible the development of topographic selective etching processes.

This concept is proposed for spacer etching process development where Si_3N_4 horizontal surface must be etched with extremely high selectivity over the vertical Si_3N_4 surface (spacer sidewalls) and underlying silicon. For this particular application, a cycling process comprising an H_2 or He plasma implantation (ion energy of about 120 eV) and a $\text{He}/\text{NH}_3/\text{NF}_3$ remote plasma process at 100 °C has been developed.

Etching mechanisms in remote plasma are really complex since they are driven by the molecules that are formed during the diffusion process from the plasma generation region to the substrate region. Gas phase characterizations would be needed to identify the reactive neutrals involved in the mechanisms and to complete a reaction scheme. However, consistent with other studies, our data confirm that the etching of the Si_3N_4 film in $\text{He}/\text{NF}_3/\text{NH}_3$ RP proceeds with the formation of $(\text{NH}_4)_2\text{SiF}_6$ salts. We propose a reaction path for this salt formation on the Si_3N_4 surface in which oxygen plays a key role. Si_3N_4 can be turned into $(\text{NH}_4)_2\text{SiF}_6$ salt only if the Si is previously oxidized explaining why the Si_3N_4 etching upon NH_3/NF_3 exposure only starts if Si-O bonds are present at the Si_3N_4 surface. Once the etching is initiated, the water released by the reaction plays the role of Si oxidant, which allows the reaction to be pursued.

Thanks to *in situ* kinetic ellipsometry, we also highlight that there is an incubation time before the salts form and the Si_3N_4 etching starts. This incubation time depends on the surface state and can be modified with surface treatment. For instance, the incubation time on a pristine Si_3N_4 with its native oxide is of 70 s, while it is reduced to 11 s and 27 s after H_2 and He implantation, respectively.

Indeed, He or H_2 implantation modifies the SiN surface state by incorporating oxygen contaminants coming from the reactor wall and creating dangling bonds. In the case of H_2 implantation, it is likely that H-terminal bonds are also created at the near surface. This functionalization considerably activates the adsorption and reaction of the neutral species generated by the $\text{He}/\text{NH}_3/\text{NF}_3$ remote plasma and thus reduces the incubation period compared to a pristine Si_3N_4 .

By adjusting properly the RP step processing time (typically 30 s) of the cycling process, implanted Si_3N_4 surface (horizontal surface) are etched with infinite selectivity over the nonimplanted Si_3N_4 surfaces (vertical surface). The two steps are repeated until

reaching the targeted Si_3N_4 thickness to be removed. It is also demonstrated that the cycling process can be stopped on the underneath Si surface with infinite selectivity and without introducing surface damage (free of residues or contamination), which is also a key criteria for spacer etching applications.

One weakness of the process is its low etch selectivity over SiO_2 films.

Those preliminary results give an overview of how powerful the reactor prototype is for the development of selective etching processes. Remote plasma processes are already known and have been used for their capability to provide highly isotropic etching selectivity, thanks to the chemical and isotropic actions of the neutrals present in the gas phase. But the implementation of this technology in a cycling process alternating a functionalization step and a remote plasma etching step offers a wide variety of selective process development. If topographically selective etching is needed, the functionalization step should involve a treatment step presenting an anisotropic character such as the ion implantation. It should be noted that a multitude of possibilities could be envisaged for the plasma chemistry (O_2 , N_2 , and CH_4) used for the implantation as long as no severe sputtering is induced. For instance, we could think of using an O_2 implantation to oxidize a material on a well-defined depth and developing a selective RP removal step of the oxide layer over the nonoxidized layer, and cycling those two steps until etching the targeted thickness. One could also imagine that the functionalization step using plasma implantation has an inhibiting effect on the next RP etching, allowing the etching of vertical surfaces selectively over horizontal surfaces.

If chemical selective etching with no preferential direction is needed, the functionalization step should use an isotropic treatment involving neutrals only that could be achieved with the remote plasma unit. We recently proposed such an approach to the isotropic and selective removal of SiGe relative to Si in order to fabricate horizontal stacked-Si nanowires for Gate All Around devices.⁵⁰

ACKNOWLEDGMENTS

This work was partly supported by LabEx Minos (No. ANR-10-LABX-55-01) and by the French RENATECH network. The authors would like to acknowledge Applied Materials for their technical support.

REFERENCES

- ¹R. Clark, K. Tapily, K.-H. Yu, T. Hakamata, S. Consiglio, D. O'Meara, C. Wajda, J. Smith, and G. Leusink, *APL Mater.* **6**, 058203 (2018).
- ²T. Faraz, F. Roozeboom, H. C. M. Knoops, and W. M. M. Kessels, *ECS J. Solid State Sci. Technol.* **4**, N5023 (2015).
- ³K. J. Kanarik, S. Tan, and R. A. Gottscho, *J. Phys. Chem. Lett.* **9**, 4814 (2018).
- ⁴A. Chaker, C. Vallee, V. Pesce, S. Belahcen, R. Vallat, R. Gassilloud, N. Posseme, M. Bonvalot, and A. Bsiesy, *Appl. Phys. Lett.* **114**, 043101 (2019).
- ⁵A. J. M. Mackus, M. J. M. Merkx, and W. M. M. Kessels, *Chem. Mater.* **31**, 2 (2019).
- ⁶B. E. E. Kastenmeier, P. J. Matsuo, and G. S. Oehrlein, *J. Vac. Sci. Technol. A* **17**, 3179 (1999).
- ⁷S. Lee, J. Oh, K. Lee, and H. Sohn, *J. Vac. Sci. Technol. B* **28**, 131 (2010).
- ⁸K. Eriguchi, A. Matsuda, Y. Nakakubo, M. Kamei, H. Ohta, and K. Ono, *IEEE Electron Device Lett.* **30**, 712 (2009).
- ⁹R. Blanc, F. Leverd, T. David, and O. Joubert, *J. Vac. Sci. Technol. B* **31**, 051801 (2013).
- ¹⁰R. Blanc, F. Leverd, M. Darnon, G. Cunge, S. David, and O. Joubert, *J. Vac. Sci. Technol. B* **32**, 021807 (2014).
- ¹¹C. Petit-Etienne, E. Pargon, S. David, M. Darnon, L. Vallier, O. Joubert, and S. Banna, *J. Vac. Sci. Technol. B* **30**, 040604 (2012).
- ¹²C. Petit-Etienne, M. Darnon, L. Vallier, E. Pargon, G. Cunge, F. Boulard, O. Joubert, S. Banna, and T. Lill, *J. Vac. Sci. Technol. B* **28**, 926 (2010).
- ¹³N. Posseme, O. Joubert, and L. Vallier, U.S. patent 9,570,317 B2 (December 20, 2013).
- ¹⁴N. Posseme, O. Pollet, and S. Barnola, *Appl. Phys. Lett.* **105**, 051605 (2014).
- ¹⁵O. Pollet, N. Possémé, V. Ah-Leung, and M. Garcia Barros, *Solid State Phenom.* **255**, 69 (2016).
- ¹⁶V. Ah-Leung, O. Pollet, N. Possémé, M. Garcia Barros, N. Rochat, C. Guedj, G. Audoit, and S. Barnola, *J. Vac. Sci. Technol. A* **35**, 021408 (2017).
- ¹⁷N. Posseme, V. Ah-Leung, O. Pollet, C. Arvet, and M. Garcia-Barros, *J. Vac. Sci. Technol. A* **34**, 061301 (2016).
- ¹⁸H. Nishino, N. Hayasaka, and H. Okano, *J. Appl. Phys.* **74**, 1345 (1993).
- ¹⁹S. D. Sherpa and A. Ranjan, *J. Vac. Sci. Technol. A* **35**, 01A102 (2017).
- ²⁰S. D. Sherpa, P. L. G. Ventzek, and A. Ranjan, *J. Vac. Sci. Technol. A* **35**, 05C310 (2017).
- ²¹V. Martirosyan, E. Despiau-Pujo, J. Dubois, G. Cunge, and O. Joubert, *J. Vac. Sci. Technol. A* **36**, 041301 (2018).
- ²²P. J. Cumpson, *J. Electron Spectrosc. Relat. Phenom.* **73**, 25 (1995).
- ²³H. Ogawa, T. Arai, M. Yanagisawa, T. Ichiki, and Y. Horiike, *Jpn. J. Appl. Phys.* **41**, 5349 (2002).
- ²⁴A. Tavernier, L. Favennec, T. Chevolleau, and V. Jousseume, *ECS Trans.* **45**, 225 (2012).
- ²⁵H. J. Oh, J. H. Lee, M. S. Lee, W. G. Shin, S. Y. Kang, G. D. Kim, and D. H. Ko, *ECS Trans.* **61**, 1 (2014).
- ²⁶A. R. Forouhi and I. Bloomer, *Phys. Rev. B* **34**, 7018 (1986).
- ²⁷J. G. E. Gardeniers, H. A. C. Tilmans, and C. C. G. Visser, *J. Vac. Sci. Technol. A* **14**, 2879 (1996).
- ²⁸J. F. Ziegler, *The Stopping and Range of Ions in Solids* (Pergamon Press, New York, 1985).
- ²⁹M. Bizouerne, E. Pargon, C. Petit-Etienne, S. Labau, S. David, M. Martin, and P. Burtin, *J. Vac. Sci. Technol. A* **36**, 061305 (2018).
- ³⁰See <https://physics.nist.gov/physrefdata/ASD/ionenergy.html> for ionization energy for He I and O I.
- ³¹K. Suzuki, R. Sudo, and T. Feudel, *Solid State Electron.* **42**, 463 (1998).
- ³²J. F. Gibbons and S. Mylroie, *Appl. Phys. Lett.* **22**, 568 (1973).
- ³³M. J. Kushner, *J. Appl. Phys.* **58**, 4024 (1985).
- ³⁴V. Martirosyan, "Atomistic simulations of H_2 and He plasmas modification of thin-films materials for advanced etch processes," Ph.D. dissertation (UGA, 2017). See <https://tel.archives-ouvertes.fr/tel-01803013>.
- ³⁵T. Hayashi, K. Ishikawa, M. Sekine, M. Hori, A. Kono, and K. Suu, *Jpn. J. Appl. Phys.* **51**, 016201 (2012).
- ³⁶W. R. Knolle and R. D. Huttemann, *ECS J. Solid State Sci. Technol.* **135**, 2574 (1988).
- ³⁷D. L. Flamm, *Pure Appl. Chem.* **62**, 1709 (1990).
- ³⁸G. Ehrlich, *J. Phys. Chem.* **59**, 473 (1955).
- ³⁹J. A. Becker and C. D. Hartman, *J. Phys. Chem.* **57**, 153 (1953).
- ⁴⁰D. M. Knotter, *J. Am. Chem. Soc.* **122**, 4345 (2000).
- ⁴¹D. M. Knotter and T. J. J. D. Denteneer, *J. Electrochem. Soc.* **148**, F43 (2001).
- ⁴²W.-H. Kim, F. S. Minaye Hashemi, A. J. M. Mackus, J. Singh, Y. Kim, D. Bobb-Semple, Y. Fan, T. Kaufman-Osborn, L. Godet, and S. F. Bent, *ACS Nano* **10**, 4451 (2016).
- ⁴³F. S. Minaye Hashemi, B. R. Birchansky, and S. F. Bent, *ACS Appl. Mater. Interfaces* **8**, 33264 (2016).
- ⁴⁴M. Leskelä and M. Ritala, *Angew. Chem. Int. Ed.* **42**, 5548 (2003).

⁴⁵B. A. Thedjoworo, D. Cheung, and D. Zamani, *J. Vac. Sci. Technol. A* **30**, 031303 (2012).

⁴⁶Z. Donkó, A. Derzsi, M. Vass, J. Schulze, E. Schuengel, and S. Hamaguchi, *Plasma Sources Sci. Technol.* **27**, 104008 (2018).

⁴⁷S. Kumakura, M. Tabata, and M. Honda, *Jpn. J. Appl. Phys.* **58**, SEEB01 (2019).

⁴⁸R. Alfonsetti, L. Lozzi, M. Passacantando, P. Picozzi, and S. Santucci, *Appl. Surf. Sci.* **70–71**, 222 (1993).

⁴⁹S. Sato, I. Mizushima, K. Miyano, T. Sato, S. Nakamura, Y. Tsunashima, T. Arikado, and N. Uchitomi, *Jpn. J. Appl. Phys.* **44**, 1169 (2005).

⁵⁰E. Pargon, C. Petit-Etienne, L. Youssef, G. Thomachot, and S. David, *J. Vac. Sci. Technol. A* **37**, 040601 (2019).